Preprint Title	Intermodal coupling spectroscopy of mechanical modes in micro-cantilevers
Authors	Ioan Ignat, Bernhard Schuster, Jonas Hafner, MinHee Kwon, Daniel Platz and Ulrich Schmid
Publication Date	26 Sep. 2022
Article Type	Full Research Paper
ORCID® iDs	Ioan Ignat - https://orcid.org/0000-0003-2462-6692; Ulrich Schmid - https://orcid.org/0000-0003-4528-8653

Intermodal coupling spectroscopy of mechanical modes in micro-cantilevers

Ioan Ignat*[1], Bernhard Schuster[1], Jonas Hafner[1], MinHee Kwon[1], Daniel Platz[1] and Ulrich Schmid[1, 1]

Address: [1]Institute of Sensor and Actuator Systems, TU Wien, Gußhaustraße 27-29, 1040 Vienna, Austria

Email: Ioan Ignat - ioan.ignat@tuwien.ac.at

* Corresponding author

Abstract

Atomic force microscopy (AFM) is highly regarded as a lens peering into the next discoveries of nanotechnology. Fundamental research in atomic interactions, molecular reactions and biological cell behaviours are key focal points, demanding a continuous increase in resolution and sensitivity. While renowned fields such as optomechanics have marched towards outstanding signal-to-noise ratios, these improvements have yet to find a practical way to AFM. Here we investigate a mechanism as a solution where individual mechanical eigenmodes of a micro-cantilever couple to one another, mimicking optomechanical techniques of reducing thermal noise. We have a look at the most commonly used modes in AFM. Starting with the first two flexural modes of cantilevers and asses the impact of an amplified coupling between them. Following, we expand our investigation to the sea of eigenmodes available in the same structure and find a maximum coupling of 9.38×10^3 Hz/nm between two torsional modes. Through such findings we aim to expand the field of multi-frequency AFM with innumerable possibilities leading to improved signal-to-noise ratios, all accessible with no additional hardware.

Keywords

atomic force microscopy; optomechanics; intermodal coupling; sideband cooling; nonlinear mechanics

Introduction

Atomic force microscopy has established itself as one of the most powerful tools in nanotechnology. With meticulous setups amassing techniques such as ultra high vacuum, cryogenic temperatures and CO-terminated tips, it is able to create a wonderful vista of surfaces, not missing the atoms for the topographical features [1-6]. There is, however, room for improvement in cutting edge AFM experiments, as the standard quantum limit in sensitivity, represented by a minimum between detection noise and backaction noise, has not been reached [7,8]. Beyond it, techniques exist that can even break this quantum barrier by redirecting noise from one quadrature to another [9-11]. Yet there is even opportunity in revitalising the accessibility of standard AFM, as performing experiments at cryogenic temperatures and under ultra-high vacuum [12,13] requires years of expertise.

For inspiration, we turn to quantum optomechanics and its sister field of quantum electromechanics, as they both report outstanding signal-to-noise ratios [14]. In the former a reflective mechanical resonator constitutes half of a Fabry-Pérot cavity, converting photons to phonons and vice versa. Thus, the mechanical position can be read through the optical cavity. Upon this basic interaction, many emerging behaviours were found: sideband cooling down to quantum levels [15,16], parametric amplification [17] before signal detection, state squeezing [18-20] and Bogoliubov modes [21,22] for drastically reducing noise and directional amplifiers [23,24]. The group of proposed applications is even larger and hosts ideas such as quantum circulators [23,24], Ising model simulators [25] and improved gravity wave detection experiments [8]. All these techniques can be migrated to AFM, with the main hurdle being the integration of an optical Fabry-Pérot cavity with an elastic micro-cantilever. We chose to use purely mechanical coupling, an alternative mirroring our source of inspiration. It relies on non-linear elastic coupling between different vibrational eigenmodes of a mechanical resonator. As the stress field of one mode stiffens the vibrational motion of another, an energy exchange is established between them. We will refer to this phenomena as intermodal coupling. It allows us to replace the optical cavity from optomechanics with a mechanical eigenmode.

So far, intermodal coupling was proven in doubly clamped beams and square membranes [18,26,27]. Both difficult geometries to base an atomic force microscope around due to the angle requirement between the probe and sample. In the following, we will explore intermodal coupling in a micro-cantilever as an opportunity to bring optomechanical techniques to AFM. It is easily accessible, with no hardware modifications and only requiring multifrequency excitation [28-32] applied to the cantilever by either a piezoshaker or modulated laser, found in many AFM setups. Intermodal coupling requires a strong drive tone, referred to as a pump, at either the frequency difference or sum between two cantilever eigenmodes of interest. Using the difference, also known as a red sideband or anti-Stokes pump, leads to sideband cooling and mode splitting. Applying the sum, referred as blue sideband pump, will cause either mode squeezing of parametric amplification[22], provided that the amplitude is optimally chosen. We will focus on the red sideband, as sideband cooling is useful for reducing thermal noise in standard AFM and mode splitting is a good way to measure the coupling rates. Here, the phonons from the first mode will have their frequency upconverted to the same as the second mode's phonons, thus allowing them to interact. This pump effectively amplifies the single phonon-phonon coupling rate of the mode combination and linearly increases the overall coupling strength $G_{ij} = G^0_{ij} X_{pump}$, where X_{pump} is the pump amplitude, thus giving us the following Hamiltonian for two coupled eigenmodes

$$\begin{aligned} H_{ij} = &\underbrace{\frac{1}{2}(G^0_{ij} + G^0_{ji}) X_i X_j X^{\text{pump}}_{ij} \cos((\omega_i - \omega_j)t) +}_{\text{interaction}} \\ &\underbrace{\frac{1}{2}(m_i^{\text{eff}} \omega_i^2 X_i^2 + m_j^{\text{eff}} \omega_j^2 X_j^2)}_{\text{energy of the modes}} + \underbrace{V_{\text{sense}} X_i \cos(\omega_{\text{sense}} t)}_{\text{amplification signal}}, \end{aligned} \tag{1}$$

where ω_i and ω_j are the frequencies of the i$^{\text{th}}$ mode, henceforth known as the sense mode, and j$^{\text{th}}$ mode, taking the role of the cavity mode in cavity optomechanics, respectively. X_i and X_j are their amplitudes, X_{ij}^{pump} the amplitude of the pump, G_{ij}^0 and G_{ji}^0 are the directional single phonon-phonon parametric coupling rates. The last term describes a small signal V_{sense}, with the frequency swept close to ω_i, used to amplify the spectral response of the sense mode above the thermal excitation level.

The above Hamiltonian is a modified version of the one used in reference [26]. In contrast to this previous work, we don't exclude the possibility of asymmetrical coupling. This refers to an energy transfer either easier or harder from first mode to second compared to from second to first. Two directional coupling terms were introduced to account for this possibility, later to be investigated in detail. Equation 1 only shows the energy of two modes and their interaction, amplified by the red sideband pump, which is set at the frequency difference of the two modes in question. A main advantage of working with continuous mechanical systems, such as micro-cantilevers, is the plethora of eigenmodes available [33]. For every combination of two eigenmodes, a pump frequency can be applied to activate that intermodal coupling. Thus, the Hamiltonian can be expanded to include more eigenmode combinations including their individual energies as well as the interaction terms (the latter is only relevant if a pump is applied). We will focus only on a finite number of eigenmodes due to our equipment limitations. The full Hamiltonian is given by

$$H = \sum_{i \neq j} \frac{1}{2} G_{0ij} X_i X_j X_{ij}^{\text{pump}} \cos((\omega_i - \omega_j)t + \sum_i \frac{1}{2} m_i^{\text{eff}} \omega_i^2 X_i^2 + V_{\text{sense}} X_i \cos(\omega_{\text{sense}} t). \qquad (2)$$

If this coupling is a direct analog to optomechanics, the coupling matrix should be symmetric, i.e. $G_{ij}^0 = G_{ji}^0$. Expanding the experiment to multiple eigenmodes will elucidate if this symmetry is respected or not in these purely mechanical interactions, and provide a spectroscopy map of intermodal coupling.

The coupling presented so far, using a red sideband signal, has two ways for manifesting itself: sideband cooling, where the mode of interest has its quality factor reduced alongside its effective temperature; and mode splitting, where two hybridised eigenmodes replace the original. The latter is useful in estimating the coupling strength, but the former is more applicable to AFM. It can not only control the quality factor of cantilevers, but it can also reduce the thermal noise of the measurement. These two behaviours have a regime assosicated to each. The i$^{\text{th}}$ mode, as the sense mode, is in the weak regime if G_{ij} is smaller than $\Gamma_j/2$, the linewidth of the cavity mode. In this case it's susceptibility (spectral response) can be written as

$$|\chi_i(\delta)|^2 = \sqrt{\Gamma_i}\frac{\Gamma_j/2 + i\delta}{(\Gamma_i/2 + i\delta)(\Gamma_j/2 + i\delta) + G_{ij}^2} \tag{3}$$

where δ is the frequency offset from the eigenfrequency ω_1, Γ_1 and Γ_2 are the linewidths of the modes. The equation can be further simplified to a Lorentzian with an increasing effective linewidth as per equation $\Gamma_i^{\text{eff}} = \left(1 + 4G_{ij}^2/(\Gamma_i\Gamma_j)\right)\Gamma_i$, enabling us to extract the coupling strength. If $G_{ij} > \Gamma_j/2$, the sense mode is in the strong regime. Here the susceptibility equation is

$$|\chi_i(\delta)|^2 = \frac{\Gamma_i/4}{\frac{(\Gamma_j+\Gamma_i)}{4}^2 + (\delta + G_{ij})^2} + \frac{\Gamma_i/4}{\frac{(\Gamma_j+\Gamma_i)}{4}^2 + (\delta - G_{ij})^2}, \tag{4}$$

In this case, the distance between peaks can be approximated as $\Delta = G_{ij}/\pi$.
The effective temperature of the mode is calculated by normalizing the integral of the measured amplitude squared to the case when the pump is off when the system is at room temperature as follows:

$$T_{\text{effective}} = \frac{\int_{\delta_{\text{start}}}^{\delta_{\text{end}}} X^2(\delta, V_{\text{pump}})d\delta}{\int_{\delta_{\text{start}}}^{\delta_{\text{end}}} X^2(\delta, 0)d\delta} T_{\text{ambient}}, \tag{5}$$

where X is the spectral response amplitude w.r.t. frequency offset from eigenfrequency δ and pump amplitude V_{pump}, T_{ambient} is the temperature of the room where experiment was performed, δ_{start} and δ_{end} are the start and end frequencies, respectively, of the lock in measurement.

An AFM micro-cantilever (Bruker RFESP-75) is glued to a piezoshaker and placed in a vacuum chamber (0.5×10^{-7}mbar) under a laser Doppler vibrometer (LDV) (Polytech MSA 500) to measure the cantilever's resonance frequencies and mode shapes 1. A lock-in amplifier (Intermodulation Products MLA-3) is used to control the piezoshaker and measure multiple frequencies from the vibrometer. For each possible mode combination, we activated the anti Stokes pump and used a smaller sweeping signal to amplify the sense mode.

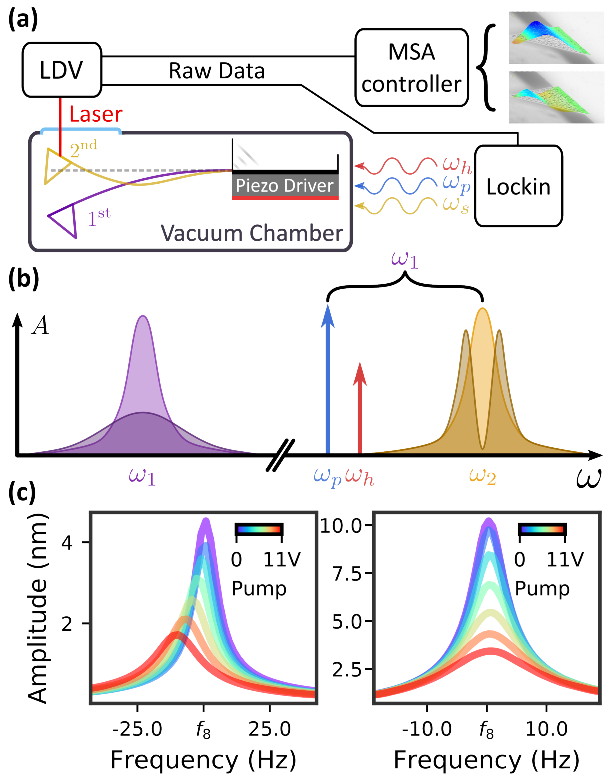

Figure 1: (a) Schematic drawing of the experimental setup. The cantilever is glued to the macro-sized piezo driver. The LDV can either send data to the MSA to determine the eigenmode shapes, or to the lock-in for higher bandwidth measurements. The latter also synthesises the signal applied to the piezo driver. **(b)** Schematic of the signals used. Three signals are in effect at all times: the red sideband pump, an offseted red sideband pump ensuring even heating across the data set and a small one, compared to the previous, sweeping over the sense mode. **(c)** Example of a two signal measurement (left) versus a three signal measurement (right), ensuring thermal stabilisation. The sum of heating signal and pump is constant.

Results and Discussion

Compared to a plain micro-cantilever, one with an AFM tip has certain peculiarities to it. The table below 1 shows the eigenmodes and their frequencies of the modes of interest in the cantilever used, measured using a LDV. Alongside it, on th last column, we performed FEM simulation estimations for the frequencies. The appearance of multiple torsional modes of same order was observed experimentally on multiple cantilevers, but could not be replicated with a simple FEM model. Figure 2 shows a comparison between the two third order torsional modes present in the cantilever (T3 and T3'). The anomalous one, T3', unseen in the FEM simulations, has the nodal lines much closes to the added mass. The other orders were observed below the frequency of T3', but they were much harder to excite with the piezoshaker used for the experiment, and therefore excluded from the analysis. The existence of these modes can be explained through a combination of the extra mass of the AFM tip on the cantilever and material differences in the silicon caused by fabrication processes.

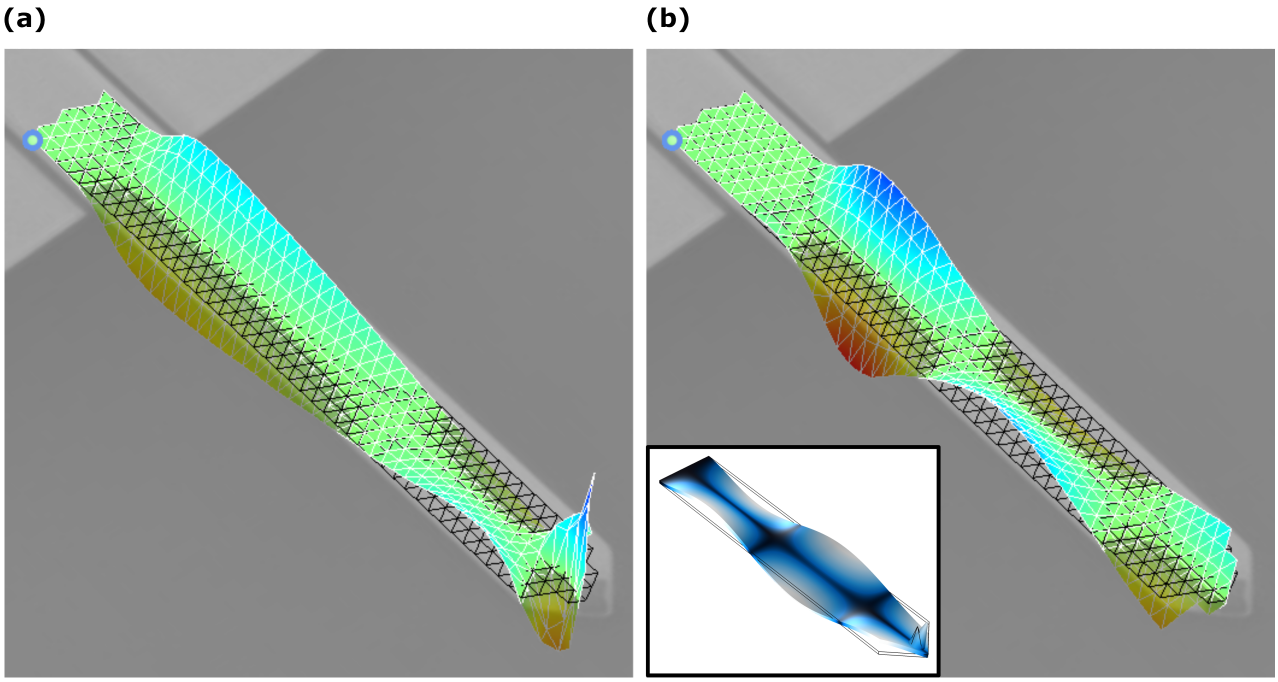

Figure 2: MSA measurements showing the difference in modeshapes between the third order torsional modes investigated in the main text. **(a)** is T3' with a node much closer to the added mass of the tip. **(b)** is T3, with nodes closer to their expected positions. **Inset:** FEM simulation of T3 eigenmode.

Table 1: Table showing the eigenmodes, their frequencies accompanied by the Q factors of the modes used in the study. Cantilever investigated is Bruker AFM RFESP-75

Eigenmode	Frequency (kHz)	Q factor	FEM frequency estimation (kHz)
first flexural (F1)	62.026	106149	62.176
second flexural (F2)	390.320	57227	388.35
first torsional (T1)	701.158	113437	704.17
anomalous third torsional (T3')	905.237	3324	-
third flexural (F3)	1096.585	3974	1085.5
second torsional (T2)	2146.963	32469	2150.2
fourth flexural (F4)	2154.353	6259	2122.9
fifth flexural (F5)	3567.223	3842	3497.8
third torsional (T3)	3710.387	46290	3703.6

After determining the modes available for measurement in the cantilever, we can focus on interaction between any two. Once a combination of modes is chosen, we focus on each mode separately as the sense mode. We measure their resonance frequencies just before performing the experiment, thus excluding shifts caused by vacuum changes or temperatures fluctuations. We stabilise for any heating effect caused by the high-voltage pump applied to the piezo shaker by adding a temperature stabilisation tone with an offset of around 3 kHz, or more if the linewidth of the sense mode becomes comparable. This second pump is set up such that it does not amplify the intermodal coupling, as the chosen offset is larger than all linewidths observed during the investigation. Thus, any products of the pump and another eigenfrequency would not coincide with another eigenmode. This temperature stabilistion tone does have a very similar heating effect as the red sideband pump. Keeping the sum of the voltages applied to the piezoshaker constant, will ensure that the heating power introduced in the system does not change when increasing the pump. Figure 1(c) shows an example on the effects of such a stabilisation approach, where the eigenfrequency does not shift lower due to thermal length extension of the cantilever. Next, we send a small frequency sweeping signal to measure the susceptibility of the sense mode.

First, we investigate the first possible mode combination on our cantilever: first and second flexural modes. In figure 3 (a) we sweep a small signal across the first mode. Each line was measured for a single value of the pump amplitude. As the amplitude of the pump increases, the linewidth does as well while the amplitude decreases as per equation 3. We calculate the effective temperature using equation (5) and we achieve a reduction down to just below 100K. The results of this evaluation are seen in figures 3 (a) inset. This data set also exhibits a significant frequency shift, as it was done without the thermal stabilisation technique described above.

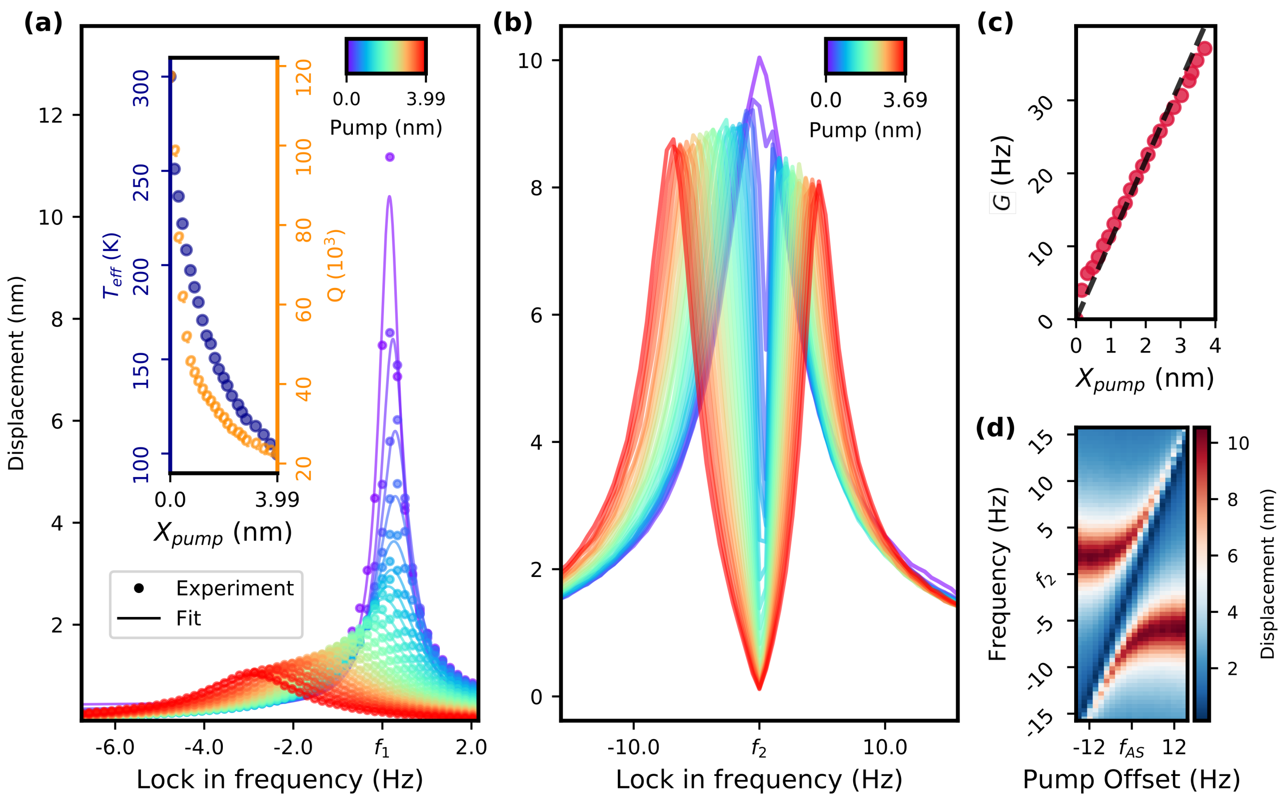

Figure 3: **(a)** Measurements of the first mode coupled with the second. Increasing the pump presents both a shift in the frequency and a reduction in effective temperature. **Inset:** Effective temperature and Q factor as a function of the pump amplitude. **(b)** Data of the second mode under different pump settings. Mode shapes under increasing amplitude of the pump. **(c)** Estimation of the coupling strength from data in (b). Slight deviations from the linear fit are caused by the approximation used. **(d)** Colormap of second mode for different frequency offsets of the pump at fixed amplitude. f_{AS} refers to the anti-Stokes pump frequency.

Keeping the pump constant while sweeping the signal tone over the second mode, we have an example of the strong coupling regime, seen in figure 3 (b). As soon as the pump is turned on, there are two distinguishable hybridised eigenmodes in lieu of the original. Increasing it further ensures that the two peaks are resolved, as the local minimum in the middle decreases and the two maxima drift further apart. The coupling strength is estimated using the frequency difference between the two peaks, as in equation's 4 approximation, and presented in figure 3 (c). With the current setup we achieved a coupling rate of 37.1 Hz. Deviations from the linear fit line starting from the origin are a direct cause of the approximation. It forgoes the interference between the hybridised modes around the original eigenfrequency, which pushes their peaks further apart the closer they are. Therefore coupling values at lower pump amplitudes are overestimated. Figure 3 (d) shows an amplitude colormap of the same mode for different frequency detunings of the anti-Stokes pump. The higher the detuning, the greater the difference in amplitude between the two peaks. As expected from an avoided mode crossing, the minimum distance between the two hybridised eigenmodes happens when the pump frequency equals the difference frequency between the modes' resonance frequencies. For the rest of the data we readjusted this frequency by performing again lock-in measurements of the eigenmodes, whenever necessary to avoid any issues caused by daily thermal drift. The applications we envisioned for AFM benefit from stronger coupling rate. Therefore we extend these measurements to the first nine modes of the cantilever under test. Figure 4 shows both the lower and the higher frequency mode response of each possible combination. Coupling rate are calculated from the distance between the two hybridised modes, the increasing linewidth or both if a regime change from weak to strong can be seen, as is the case of F2-T3 (i.e., sense mode F2 with cavity mode T3). This specific case is explored further in Figure 5 (a), with an inset detailing the coupling rate values taken from the two regimes. The split measurements are overvalued due to the approximation as described previously. The inset has a horizontal line at half the linewidth of the cavity mode. The regime changes at this point as detailed before. Figure 5 (b) presents the coupling matrix, colormap containing the directional coupling strength between two modes normalised to pump amplitude in nm. The highest measured coupling rate between flexural modes is 5.15×10^2 Hz/nm. Overall the T3 and T3' showed an even higher G^0 at 9.38×10^3 Hz/nm. For comparison to literature, we need to see the dependence of the coupling strength to pump voltage used. For the same mode combination presented above, the coupling strength achieved is 5.49×10^2 Hz/V, greater by a factor of 3.4 compared to other findings[27]. Exploring the coupling map further, one can observe that for flexural modes the higher the order, the higher the coupling

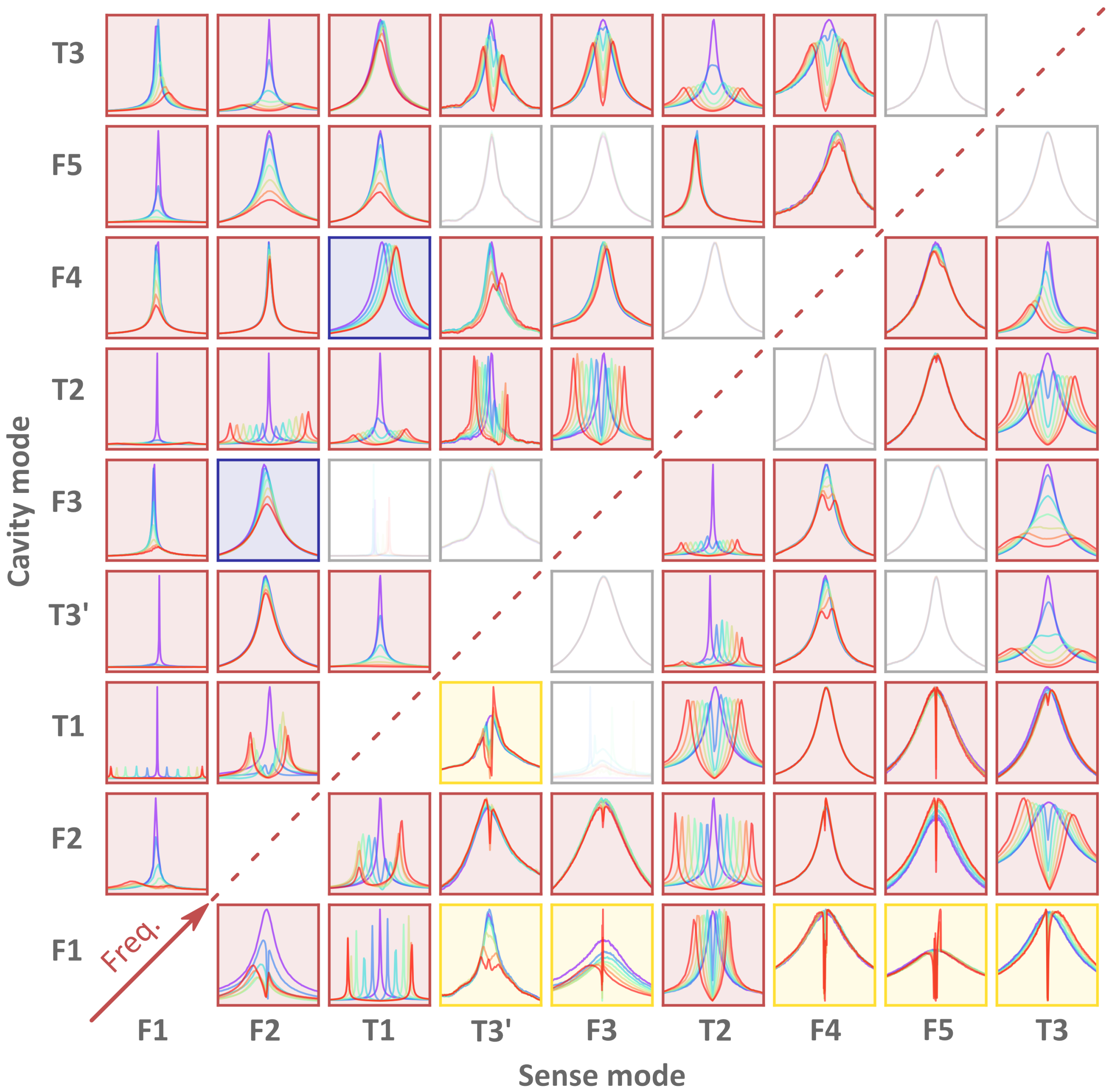

Figure 4: Map of the observed modes under anti-Stokes pumps. On the columns we have the sense mode, while the rows designate the mode it is coupled to, from bottom left. The greyed out graphs are setups where no discernible coupling is present. The red ones follow the expectation of the optomechanical Hamiltonian. The yellow ones exhibit nonlinear behaviour not described by the aforementioned Hamiltonian. Blue have a significant frequency shift unexplained by cantilever expanding under heating.

strength per nm of pump amplitude. Mode combinations which include torsional modes also see the same effect.

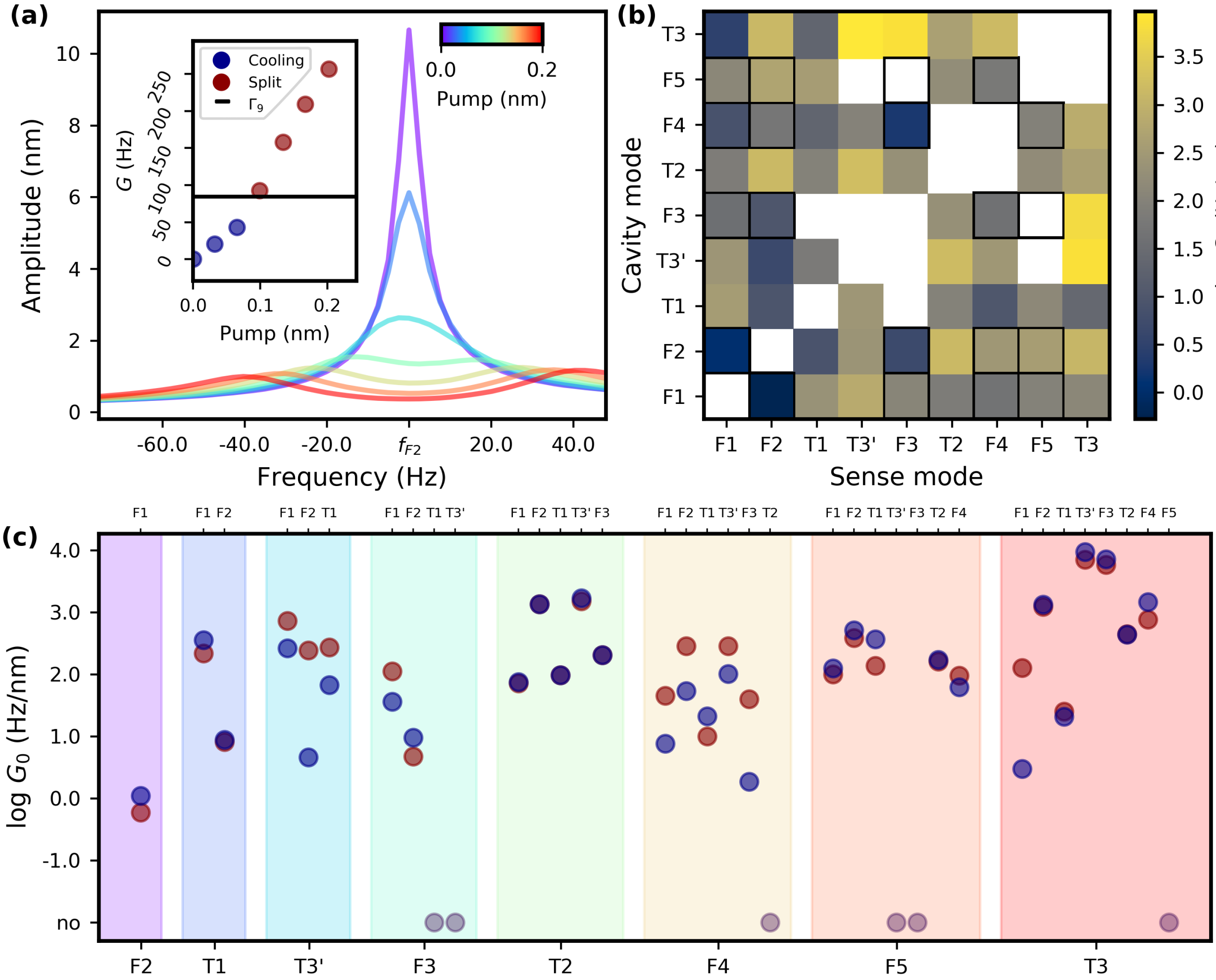

Figure 5: **(a)** Graph for mode combination F2-T3 which has a regime transition. **Inset:** Coupling rates determined from linewidth changes or eigenmode separation against half the linewidth of cavity mode T3. **(b)** Matrix showing the coupling rates of all mode combinations. Contoured squares represent combinations between flexurals modes only. **(c)** Same data as in (b) presented in a one dimensional perspective. Blue points are calculated from data sets with the sense mode lower in frequency than the cavity mode, while red are the opposite. Greyed out points have no discernible coupling.

The map is mostly filled with several exceptions, with no indication of coupling. There are multiple explanations for the empty spaces and all can have an impact on the lack of coupling. Firstly, a piezoelectric actuator can have a minimum in its response function at the pump frequency. Secondly, the intermodal coupling effect can be at a minimum in these combinations. Lastly, any visible effect might be obscured by daily thermal fluctuations and the finite time for measurements that they impose.

Coming back to the question of coupling symmetry between two modes, figure 5 (c) has the same data as (b) but in a folded perspective. Blue points represent data from lower frequency sense modes in the combination, while red the opposite. Out of 30 combinations exhibiting intermodal coupling, 19 show symmetry. Furthermore, amongst the eleven that do not present symmetric results, nine have a higher value for the coupling rate extracted from splitting data. Eight of them are far away from the approximation of two separated Lorentzian for the peaks. Improvements can be made by fitting equation 4 which lowers the estimated values for G_{ij}. This requires better temperature control to ensure no shifts occur during the pump application and the aforementioned equation applies. The piezoshaker has a different heating response with respect to the signal frequency. Equation 4 requires an anti-Stokes pump with a perfectly tuned frequency. Bringing everything in frame, there are more points that have symmetry than not. This does not exclude the possibility that some mode combinations do exhibit asymmetric coupling mechanism. Beyond the assumed interaction Hamiltonian, terms of different orders might apply.

During our investigation, nonlinear interactions were observed and presented in Figure 5 as the yellow or blue graphs. Peculiar deviations from the strong regime theory can be seen in T3'-F1,T3'-T1,F3-F1,F5-F1 and to a lesser extend in F4-F1. The effect becomes more pronounced at higher pump amplitudes, where in the vicinity of the local minimum, new peaks start to appear. This might be caused by an excitation of the cavity mode either due to proximity to the pump signal or electrical sideband of the sense and the pump signals. Another possibility is an eigenmode not within the combination being excited by the red sideband pump, leading to a pump amplitude comparable to the sensing amplitude. Both lead to an unstable regime for the amplitude of the cavity mode. Having another eigenmode as the pump was slightly explored before [18], yet its linewidth was not taken in consideration.

Another nonlinear effect can be observed in T3-F1. Here, the local minimum decreases with the pump as expected, yet the two hybridised peaks are asymmetric in their lineshape. The one on the left having a shear drop in amplitude towards the dip, while the right one missing such feature. Lastly T1-F4 has a frequency shift. This is not uncommon in the measured data as F1-T3, F1-F3 and F3-F4 show it. Heating effects would cause a quadratic shift with respect to the pump voltage, dominated by cantilever's thermal length extension, either up or down due to the extra signal used compensating. In contrast, the frequency shift of T1-F4 is linear. A cause of this can be a different coupling term of higher order involving the mode energies directly. The same effect might be found in F2-F3 alongside a significant quadratic heating effect, causing a maximum in the frequency shift.

Throughout these measurements, the sensing voltage was carefully tuned as to not bring any of the modes in the Duffing regime.

Conclusions

We investigated the purely mechanical coupling capabilities of a typical AFM cantilever. For this purpose, we used a pump set at the frequency difference between two mechanical modes of interest. Repeating the procedure for all possible combinations of the observable eigenmodes creates a modal coupling map of the micro-resonator. Each is calibrated to their amplitudes in nm to reveal preferable combinations as well as incompatible ones. Such a data set alongside knowledge of the eigenmodes themselves can help us reveal the nature of intermodal coupling. Most of the intermodal coupling data points support a symmetric coupling Hamiltonian similar to the one used in optomechanical systems. This will inevitable lead to engineered micro-resonators taking full advantage of this phenomenon.

Mapping these couplings allows one to activate multiple at the same time. Innumerable applications include those studied in optomechanics and electromechanics, as well as theoretical implementations yet to be seen in practice, all powered by phonon-phonon interactions. Not only bringing improvements to common AFM tools, but providing opportunities for higher sensitivities in the cutting edge AFM as well.

These possibilities only multiply if the mechanical-mechanical interactions were only one aspect of a device. In a MEMS or NEMS device, such interactions would be useful to bridge electrical modes together, opening up the possibility of creating transducers mediated by a moving capacitor. Such thoughts open the doors to sensors with qualities overshadowing their predecessors.

Acknowledgements

We would like to thank the QAFM team for insightful and detailed disscussions on the topic: D. Haviland, E. Arvidsson, A. Roos, E. Scarano, T. Glatzel, M. Zutter. From Intermodulation Products, E. Tholén, D. Forchheimer provided us with outstanding support in programming the MLA-3 lockin amplifier.

Funding

This project has received funding from the European Union's Horizon 2020 research and innovation programme under grant agreement No 828966.

References

1. Giessibl, F. J. *Science* **1995**, *267* (5194), 68–71. doi:10.1126/science.267.5194.68.

2. Hembacher, S.; Giessibl, F. J.; Mannhart, J.; Quate, C. F. *Physical Review Letters* **2005**, *94* (5), 056101. doi:10.1103/PhysRevLett.94.056101.

3. Gross, L.; Mohn, F.; Moll, N.; Liljeroth, P.; Meyer, G. *Science* **2009**, *325* (5944), 1110–1114. doi:10.1126/science.1176210.

4. Ebeling, D.; Zhong, Q.; Ahles, S.; Chi, L.; Wegner, H. A.; Schirmeisen, A. *Applied Physics Letters* **2017**, *110* (18), 183102. doi:10.1063/1.4982801.

5. Dagdeviren, O. E.; Götzen, J.; Hölscher, H.; Altman, E. I.; Schwarz, U. D. *Nanotechnology* **2016**, *27* (6), 065703. doi:10.1088/0957-4484/27/6/065703.

6. Mamin, H. J.; Rugar, D. *Applied Physics Letters* **2001**, *79* (20), 3358–3360. doi:10.1063/1.1418256.

7. Schreppler, S.; Spethmann, N.; Brahms, N.; Botter, T.; Barrios, M.; Stamper-Kurn, D. M. *Science* **2014**, *344* (6191), 1486–1489. doi:10.1126/science.1249850.

8. et al., B. A.; LIGO Scientific Collaboration, *New Journal of Physics* **2009**, *11* (7), 073032. doi:10.1088/1367-2630/11/7/073032.

9. Mason, D.; Chen, J.; Rossi, M.; Tsaturyan, Y.; Schliesser, A. *Nature Physics* **2019**, *15* (8), 745–749. doi:10.1038/s41567-019-0533-5.

10. Anetsberger, G.; Gavartin, E.; Arcizet, O.; Unterreithmeier, Q. P.; Weig, E. M.; Gorodetsky, M. L.; Kotthaus, J. P.; Kippenberg, T. J. *Physical Review A* **2010**, *82* (6), 061804. doi:10.1103/PhysRevA.82.061804.

11. Teufel, J. D.; Donner, T.; Castellanos-Beltran, M. A.; Harlow, J. W.; Lehnert, K. W. *Nature Nanotechnology* **2009**, *4* (12), 820–823. doi:10.1038/nnano.2009.343.

12. Kawai, S.; Glatzel, T.; Koch, S.; Such, B.; Baratoff, A.; Meyer, E. *Physical Review B* **2010**, *81* (8), 085420. doi:10.1103/PhysRevB.81.085420.

13. Fremy, S.; Kawai, S.; Pawlak, R.; Glatzel, T.; Baratoff, A.; Meyer, E. *Nanotechnology* **2012**, *23* (5), 055401. doi:10.1088/0957-4484/23/5/055401.

14. Aspelmeyer, M.; Kippenberg, T. J.; Marquardt, F. *Reviews of Modern Physics* **2014**, *86* (4), 1391–1452. doi:10.1103/RevModPhys.86.1391.

15. O'Connell, A. D.; Hofheinz, M.; Ansmann, M.; Bialczak, R. C.; Lenander, M.; Lucero, E.; Neeley, M.; Sank, D.; Wang, H.; Weides, M.; Wenner, J.; Martinis, J. M.; Cleland, A. N. *Nature* **2010**, *464* (7289), 697–703. doi:10.1038/nature08967.

16. Wilson-Rae, I.; Nooshi, N.; Zwerger, W.; Kippenberg, T. J. *Physical Review Letters* **2007**, *99* (9), 093901. doi:10.1103/PhysRevLett.99.093901.

17. Mahboob, I.; Okamoto, H.; Yamaguchi, H. *New Journal of Physics* **2016**, *18* (8), 083009. doi:10.1088/1367-2630/18/8/083009.

18. Patil, Y.; Chakram, S.; Chang, L.; Vengalattore, M. *Physical Review Letters* **2015**, *115* (1), 017202. doi:10.1103/PhysRevLett.115.017202.

19. Szorkovszky, A.; Doherty, A. C.; Harris, G. I.; Bowen, W. P. *PHYSICAL REVIEW LETTERS* **2011**, 5.

20. Kronwald, A.; Marquardt, F.; Clerk, A. A. *PHYSICAL REVIEW A* **2013**, 10.

21. Pirkkalainen, J.-M.; Damskägg, E.; Brandt, M.; Massel, F.; Sillanpää, M. *Physical Review Letters* **2015**, *115* (24), 243601. doi:10.1103/PhysRevLett.115.243601.

22. W. P. Bowen, G. J. M. *Quantum Optomechanics*; Taylor and Francis Group, 2016.

23. Malz, D.; Tóth, L. D.; Bernier, N. R.; Feofanov, A. K.; Kippenberg, T. J.; Nunnenkamp, A. *PHYSICAL REVIEW LETTERS* **2018**, 6.

24. Bernier, N. R. *NATURE COMMUNICATIONS* **2017**, 8.

25. Mahboob, I.; Okamoto, H.; Yamaguchi, H. *Science Advances* **2016**, *2* (6), e1600236. doi:10.1126/sciadv.1600236.

26. Mahboob, I.; Nishiguchi, K.; Okamoto, H.; Yamaguchi, H. *Nature Physics* **2012**, *8* (5), 387–392. doi:10.1038/nphys2277.

27. Mahboob, I.; Nier, V.; Nishiguchi, K.; Fujiwara, A.; Yamaguchi, H. *Applied Physics Letters* **2013**, *103* (15), 153105. doi:10.1063/1.4824925.

28. Garcia, R.; Herruzo, E. T. *Nature Nanotechnology* **2012**, *7* (4), 217–226. doi:10.1038/nnano.2012.38.

29. Kawai, S.; Hafizovic, S.; Glatzel, T.; Baratoff, A.; Meyer, E. *Physical Review B* **2012**, *85* (16), 165426. doi:10.1103/PhysRevB.85.165426.

30. Hutter, C.; Platz, D.; Tholén, E. A.; Hansson, T. H.; Haviland, D. B. *Physical Review Letters* **2010**, *104* (5), 050801. doi:10.1103/PhysRevLett.104.050801.

31. Borgani, R.; Haviland, D. B. *Review of Scientific Instruments* **2019**, *90* (1), 013705. doi:10.1063/1.5060727.

32. Tholén, E. A.; Platz, D.; Forchheimer, D. *Review of Scientific Instruments* **2011**, *82*, 026109. doi:10.1063/1.3541791.

33. Platz, D.; Schmid, U. *Journal of Micromechanics and Microengineering* **2019**, *29* (12), 123001. doi:10.1088/1361-6439/ab4bad. Publisher: IOP Publishing